Direct Realization of Digital Differentiators in Discrete Domain for Active Damping of LCL-Type Grid-Connected Inverter

Pan, Donghua; Ruan, Xinbo; Wang, Xuehua

Published in:
IEEE Transactions on Power Electronics

DOI (link to publication from Publisher):
10.1109/TPEL.2017.2780174

Publication date:
2018

Document Version
Accepted author manuscript, peer reviewed version

This article has been accepted for publication in a future issue of this journal, but has not been fully edited. Content may change prior to final publication. Citation information: DOI 10.1109/TPEL.2017.2780174, IEEE Transactions on Power Electronics

Direct Realization of Digital Differentiators in Discrete Domain for Active Damping of *LCL*-Type Grid-Connected Inverter

Donghua Pan, *Member*, *IEEE*, Xinbo Ruan, *Fellow*, *IEEE*, and Xuehua Wang, *Member*, *IEEE*

***Abstract*—To damp the *LCL*-filter resonance in a grid-connected inverter, the feedback of capacitor current is usually adopted, and it can be replaced by the feedback of capacitor voltage as a low-cost solution, if an accurate digital differentiator can be made. The best way for realizing such a differentiator has so far proved to be an indirect nonideal generalized integrator (GI). As a simple alternative, this paper proposes two digital differentiators, which are directly developed in the discrete domain. They are a first-order differentiator based on backward Euler plus digital lead compensator and a second-order differentiator based on Tustin plus digital notch filter. The basic idea of the proposed methods is to correct their frequency responses to match the ideal differentiator with embedded digital filters. It is shown that the proposed differentiators exhibit the same derivative performance as the nonideal-GI differentiator, and they are more attractive for digital implementations due to their direct discrete natures, compact expressions, and easy algebraic manipulations. In particular, the proposed first-order differentiator is most competitive for its general representation and simplest implementation. Finally, a 12-kW prototype is built, and experiments are performed to verify the theoretical analysis.**

***Index Terms*—Active damping, differentiator, discrete domain, grid-connected inverter, *LCL* filter.**

I. Introduction

A grid-connected inverter with an *LCL* filter has been a popular power conversion interface in distributed power generation systems [1]. The use of *LCL* filter offers a cost-effective attenuation of the switching harmonics, but it suffers from also a severe resonance problem. Passive and active solutions for damping the *LCL*-filter resonance have been extensively discussed, with the latter being favored for its high efficiency and flexibility [2]–[6]. Active damping solutions are usually realized by compensating the control loop through feeding back the filter state variables, which might be the inverter-side inductor current [5], [6], the capacitor current [7]–[12], and the grid current [13]–[15]. Among them, the capacitor current active damping (CCAD) has proved to be effective and robust with only a proportional feedback gain [16], [17]. However, measuring the capacitor current is not convenient and would take much cost, especially in high-power applications. An alternative to this issue is to compute the capacitor current from the known capacitor voltage, thus a set of current sensors can be saved.

Obviously, a differentiator is needed for the capacitor voltage active damping (CVAD). Since the resonance frequency can vary in a wide range due to the variation of grid impedance [18], an accurate derivative over a wide frequency range should be preserved for an effective damping. This imposes great challenge on the realization of digital differentiator. Generally, there are two ways to develop a digital differentiator. One way is directly discretizing the "*s*" function with proper discretization methods, which might be forward Euler, backward Euler, and Tustin [19]. The forward Euler compromises the system stability by adding unstable poles. The backward Euler, on the other hand, introduces considerable phase lag at high frequency. Tustin produces an expected 90º phase, but its infinite gain at the Nyquist frequency will cause noise amplification. The other way is emulating the "*s*" function with a continuous filter and then discretizing such filter function, which is the indirect discretizing method. High-pass filter [13]–[15] and lead-lag element [20], [21] are the most common choices. Unfortunately, the high-pass filter is subject to the large phase lag as the backward Euler method, and the lead-lag element takes effect only in a narrow frequency range.

Therefore, the main challenges of the digital differentiator lie in the large phase lag and noise amplification at high frequency. To address these issues, an indirect differentiator based on a nonideal generalized integrator (GI) is presented in [22] and [23]. By carefully tuning the damping term of the continuous nonideal GI, the infinite noise amplification is avoided at the expense of a slight phase lag at high frequency, which closely matches the characteristics of the "s" function. And these characteristics are retained in the discretized nonideal GI by applying the first-order hold (FOH) discretization method. In spite of the satisfactory derivative performance, the discretization process takes much effort, as various discretization methods have to be examined to find the

Manuscript received June 27, 2017; revised October 23, 2017; accepted November 27, 2017. This work was supported by the National Natural Science Foundation of China under Award 50837003.

D. Pan was with the State Key Laboratory of Advanced Electromagnetic Engineering and Technology, School of Electrical and Electronic Engineering, Huazhong University of Science and Technology, Wuhan 430074, China. He is now with the Department of Energy Technology, Aalborg University, Aalborg 9220, Denmark (e-mail: dop@et.aau.dk).

X. Ruan is with the State Key Laboratory of Advanced Electromagnetic Engineering and Technology, School of Electrical and Electronic Engineering, Huazhong University of Science and Technology, Wuhan 430074, China, and also with the Center for More-Electric-Aircraft Power Systems, College of Automation Engineering, Nanjing University of Aeronautics and Astronautics, Nanjing 210016, China (e-mail: ruanxb@nuaa.edu.cn).

X. Wang is with the State Key Laboratory of Advanced Electromagnetic Engineering and Technology, School of Electrical and Electronic Engineering, Huazhong University of Science and Technology, Wuhan 430074, China (e-mail: wang.xh@hust.edu.cn).

This article has been accepted for publication in a future issue of this journal, but has not been fully edited. Content may change prior to final publication. Citation information: DOI 10.1109/TPEL.2017.2780174, IEEE Transactions on Power Electronics

best one (i.e., FOH). Moreover, resulting from the sophisticated FOH method, the discretized nonideal GI is not easy to be expressed and requires substantial algebraic manipulations before putting into practice.

Driven by the demand for ease of implementation, two simple digital differentiators that directly developed in the discrete domain are proposed in this paper. The basic idea of the proposed methods is to correct the frequency responses of the direct discretized differentiators with embedded digital filters. Specifically, a first-order differentiator is constructed by incorporating a digital lead compensator into backward Euler differentiator to raise its phase at high frequency, and a second-order differentiator is formed by cascading a digital notch filter to Tustin differentiator to attenuate its infinite gain at the Nyquist frequency. Without any complicated discretization process, the usages of the proposed differentiators turn to be very straightforward. A comparison between the proposed differentiators and the nonideal-GI-based one shows that both kinds of differentiators exhibit the same derivative performance, while the former ones are advantageous for their direct discrete natures, compact expressions, and easy algebraic manipulations, which thus facilitate their applications in practice.

This paper begins with a systematic modeling of the *LCL*-type grid-conencted inverter with either CCAD or CVAD in Section II. This is followed by a brief review of the nonideal-GI differentiator in Section III. Then, the first-order and second-order differentiators are proposed in Section IV, and they are compared to the nonideal-GI-based one in Section V. Experimental results are provided to verify the effectiveness of proposed methods in Section VI. Finally, Section VII concludes this paper.

II. Modeling the *LCL*-Type Grid-Connected Inverter

Fig. 1 shows a three-phase voltage-source inverter feeding into the grid through an *LCL* filter. L_1 is the inverter-side inductor, C is the filter capacitor, and L_2 is the grid-side inductor. L_g is the grid inductance. The grid current i_2 is controlled with a proportional-integral (PI) regulator in the synchronous *dq* frame. The capacitor voltage v_C is sensed and fed to a phase-locked loop (PLL) for grid synchronization. Since the bandwidth of the PLL is usually set far lower than that of the grid current loop, the grid current loop can be evaluated independently. For the grid current control, a single loop can stabilize the system if the *LCL*-filter resonance frequency f_r is higher than one-sixth of the sampling frequency $f_s/6$ [24]–[27]. This stable region is however hard to ensure in practice, since the variation of L_g may shift f_r across $f_s/6$. In view of this, an additional damping is required to achieve a strong robustness, and it is usually realized by a proportional feedback of the capacitor current i_C [16], [17]. To avoid an extra current sensing, i_C is computed through the derivative of v_C, as shown in Fig. 1, where K_{ad} is the damping gain. Subtracting the damping term from the output of PI regulator yields the modulation reference, which is then processed by the space vector modulation (SVM) to generate the driver signal for adjusting the inverter switching.

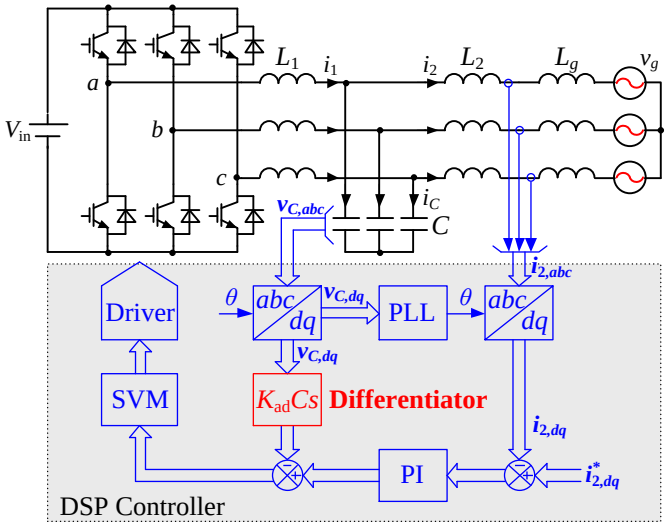

Fig. 1. Topology and current control architecture of a three-phase *LCL*-type grid-connected inverter.

The per-axis control diagram of active damping with either capacitor current or capacitor voltage is shown in Fig. 2(a), where the cross-coupling terms between the *d*-axis and *q*-axis are ignored since they have little effect on system dynamics [28]. $G_i(z)$ is the PI regulator, whose expressions before and after applying the backward Euler discretization are given as

$$G_i(s) = K_p + \frac{K_i}{s}, \quad G_i(z) = K_p + \frac{K_i T_s z}{z-1} \tag{1}$$

where K_p is the proportional gain, K_i is the integral gain, and T_s is the sampling period.

The digitally controlled system contains computation and pulse-width modulation (PWM) delays, whose total value is one and half sampling periods [29]. These delays are incorporated in Fig. 2(a). Specifically, the computation delay is one sampling period, and it is modeled as z^{-1}. The PWM delay is half sampling period, and it is caused by the zero-order hold (ZOH), which is expressed as

$$G_h(s) = \frac{1-e^{-sT_s}}{s}. \tag{2}$$

$K_{PWM} = V_{in}/(2V_{tri})$ is the transfer function of the PWM inverter, where V_{in} is the input voltage, and V_{tri} is the amplitude of the triangular carrier. $G_{ic}(s)$, $G_{vc}(s)$, and $G_{i2}(s)$ are the transfer functions from the inverter bridge output voltage $v_{inv}(s)$ to $i_C(s)$, $v_C(s)$, and $i_2(s)$, respectively, and they are expressed as

$$\begin{aligned} G_{ic}(s) &= \frac{i_C(s)}{v_{inv}(s)} = \frac{1}{L_1}\cdot\frac{s}{s^2+\omega_r^2} \\ G_{vc}(s) &= \frac{v_C(s)}{v_{inv}(s)} = \frac{1}{L_1 C}\cdot\frac{1}{s^2+\omega_r^2} \\ G_{i2}(s) &= \frac{i_2(s)}{v_{inv}(s)} = \frac{1}{s(L_1+L_2+L_g)}\cdot\frac{\omega_r^2}{s^2+\omega_r^2} \end{aligned} \tag{3}$$

where ω_r is the *LCL*-filter resonance angular frequency and expressed as

$$\omega_r = 2\pi f_r = \sqrt{\frac{L_1+L_2+L_g}{L_1(L_2+L_g)C}}. \tag{4}$$

This article has been accepted for publication in a future issue of this journal, but has not been fully edited. Content may change prior to final publication. Citation information: DOI 10.1109/TPEL.2017.2780174, IEEE Transactions on Power Electronics

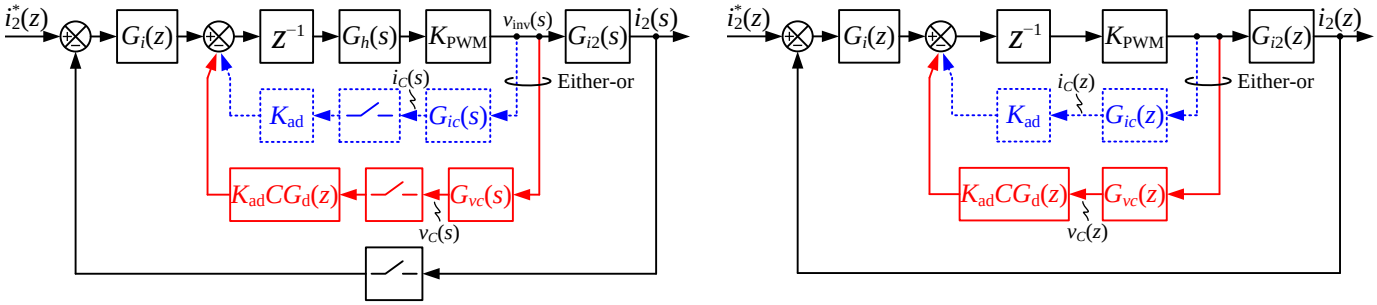

Fig. 2. Per-axis control diagram of active damping with either capacitor current or capacitor voltage. (a) Initial model. (b) Discrete model.

For digital implementation of the CVAD, the differentiator "s" is realized by a discrete function $G_d(z)$, whose performance will be discussed latter. By applying the ZOH discretization to (3), the initial model in Fig. 2(a) can be transformed into the discrete one, as shown in Fig. 2(b), where

$$G_{ic}(z)=Z_{ZOH}\left[G_{ic}(s)\right]=\frac{\sin\omega_r T_s}{\omega_r L_1}\cdot\frac{z-1}{z^2-2z\cos\omega_r T_s+1}$$
$$G_{vc}(z)=Z_{ZOH}\left[G_{vc}(s)\right]=\frac{1-\cos\omega_r T_s}{\omega_r^2 L_1 C}\cdot\frac{z+1}{z^2-2z\cos\omega_r T_s+1}$$
$$G_{i2}(z)=Z_{ZOH}\left[G_{i2}(s)\right]=\frac{\omega_r T_s\left(z^2-2z\cos\omega_r T_s+1\right)-(z-1)^2\sin\omega_r T_s}{\omega_r\left(L_1+L_2+L_g\right)(z-1)\left(z^2-2z\cos\omega_r T_s+1\right)} \quad (5)$$

Then, the system loop gains related to CCAD and CVAD, i.e., $T_{ic}(z)$ and $T_{vc}(z)$, can be derived as (6), shown at the bottom of this page.

$T_{ic}(z)$ and $T_{vc}(z)$ can be used to evaluate the effectiveness of the two active damping solutions. As depicted in (6), the digital differentiator $G_d(z)$ is essential to the equivalence between $T_{ic}(z)$ and $T_{vc}(z)$, and it is focused in the next sections. Besides, designs of the damping gain K_{ad} and PI parameters have been intensively discussed in [16] and [29], thus they are not repeated here.

III. Brief Review of Indirect Nonideal-GI Differentiator

As previously mentioned, the effectiveness of the CVAD is dependent on the accuracy of the digital differentiator. Among various digital differentiators, the indirect nonideal-GI differentiator was proved to have the best derivative performance [22], [23]. A brief review of such method is thus necessary to help construct new differentiators.

Generally, an ideal GI can be expressed as

$$G_{GI}(s)=\frac{\omega_n^2 s}{s^2+\omega_n^2}. \quad (7)$$

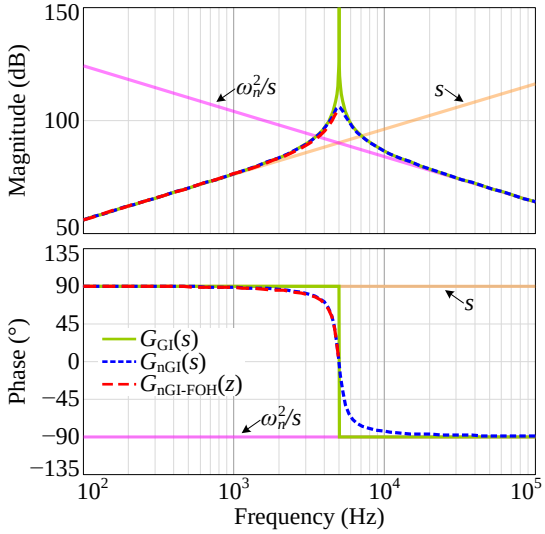

Fig. 3. Frequency responses of ideal differentiator, ideal integrator, ideal GI, nonideal GI, and FOH-discretized nonideal GI.

Note that, at frequencies lower than ω_n, $G_{GI}(s)$ can be simplified as an ideal differentiator, i.e., $G_{GI}(s)\approx s$; and at frequencies higher than ω_n, $G_{GI}(s)$ can be simplified as an ideal integrator (rescaled by ω_n^2), i.e., $G_{GI}(s)\approx\omega_n^2/s$, as shown in Fig. 3. In order to make a maximum utilization of its derivative characteristic, ω_n is set to the Nyquist frequency, which is $\omega_n=\pi\times10^4$ rad/s for 10-kHz sampling. However, with an infinite gain at ω_n, the ideal GI will suffer from the noise amplification problem. To overcome this drawback, a nonideal GI is constructed by adding a damping term $\omega_c s$ to the ideal one, i.e.,

$$G_{nGI}(s)=\frac{\omega_n^2 s}{s^2+\omega_c s+\omega_n^2}. \quad (8)$$

The gain at ω_n is now reduced to $|G_{nGI}(s)|=\omega_n^2/\omega_c$, which decreases with the increase of ω_c. A larger ω_c thus leads to a

$$T_{ic}(z)=\frac{K_{PWM}G_i(z)G_{i2}(z)}{z+K_{ad}K_{PWM}G_{ic}(z)}=\frac{K_{PWM}G_i(z)}{\omega_r\left(L_1+L_2+L_g\right)}\cdot\frac{\omega_r T_s\left(z^2-2z\cos\omega_r T_s+1\right)-(z-1)^2\sin\omega_r T_s}{(z-1)\left[z\left(z^2-2z\cos\omega_r T_s+1\right)+\frac{K_{ad}K_{PWM}\sin\omega_r T_s}{\omega_r L_1}(z-1)\right]}$$

$$T_{vc}(z)=\frac{K_{PWM}G_i(z)G_{i2}(z)}{z+K_{ad}K_{PWM}CG_d(z)G_{vc}(z)}=\frac{K_{PWM}G_i(z)}{\omega_r\left(L_1+L_2+L_g\right)}\cdot\frac{\omega_r T_s\left(z^2-2z\cos\omega_r T_s+1\right)-(z-1)^2\sin\omega_r T_s}{(z-1)\left[z\left(z^2-2z\cos\omega_r T_s+1\right)+\frac{K_{ad}K_{PWM}(1-\cos\omega_r T_s)}{\omega_r^2 L_1}(z+1)G_d(z)\right]} \quad (6)$$

This article has been accepted for publication in a future issue of this journal, but has not been fully edited. Content may change prior to final publication. Citation information: DOI 10.1109/TPEL.2017.2780174, IEEE Transactions on Power Electronics

better noise rejection, but is compromised by the increasing phase error around ω_n. ω_c = 5×10^3 rad/s is taken as a good tradeoff between noise rejection and phase error, as shown in Fig. 3. Consequently, $G_{\text{nGI}}(s)$ is taken for discretization instead of $G_{\text{GI}}(s)$.

In [22] and [23], various discretization methods had been tried, and the best one for discretizing $G_{\text{nGI}}(s)$ was found to be the FOH method, but its discretized expression was not given due to the high complexity. Here, it is derived as (9), shown at the bottom of this page. In (9), ω_d is expressed as

$$\omega_d = \sqrt{\omega_n^2 - \frac{\omega_c^2}{4}}\,. \tag{10}$$

Frequency response of $G_{\text{nGI-FOH}}(z)$ is also shown in Fig. 3. The discretized nonideal GI exhibits well-matched characteristics as the continuous one, which implies an accurate derivative performance that close to the ideal differentiator.

From the above reviewing, it can be concluded that the development of the nonideal-GI differentiator requires a careful tuning of the continuous filter to closely match the "s" function at first, and then a discretization process to totally retain its characteristics in the discrete domain. To perform a desired discretization, the sophisticated FOH method is adopted, which unfortunately complicates the discretized expression and features a heavy computation burden, as shown in (9). However, such shortcomings can be immediately avoided if a differentiator can be directly developed in the discrete domain. From this point of view, two simple digital differentiators will be constructed in the following section.

IV. Direct Realization of Digital Differentiators in Discrete Domain

Direct differentiators can be realized by applying forward Euler, backward Euler, or Tustin to the "s" function, as discussed in Section I. Since the forward Euler destabilizes the system, the backward Euler and Tustin are considered here. However, these two methods are challenged by the practical issues, such as phase lag and noise amplification. By revisiting to them, a basic idea for addressing these issues is proposed in this section.

A. Basic Idea of Proposed Differentiators

The expressions of backward Euler and Tustin differentiators are given as

$$G_{\text{back}}(z) = \frac{z-1}{zT_s},\quad G_{\text{tustin}}(z) = \frac{2}{T_s}\frac{z-1}{z+1}. \tag{11}$$

Frequency responses of $G_{\text{back}}(z)$ and $G_{\text{tustin}}(z)$ with the sampling frequency f_s = 10 kHz are shown in Fig. 4, where an ideal differentiator is also presented for comparison. As seen, each differentiator has its own attractive advantage, but also

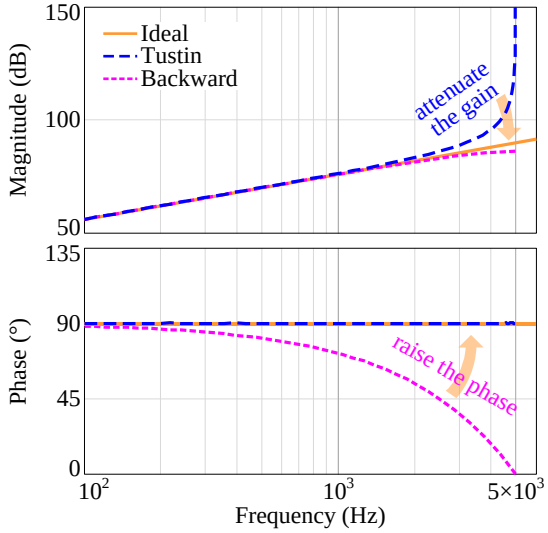

Fig. 4. Frequency responses of ideal, backward Euler, and Tustin differentiators.

faces visible disadvantage. Backward Euler differentiator yields a good magnitude response, but its phase rolls off and reaches zero as the frequency goes high. The large phase lag will cause the loss of derivative effect, which thus limits its usage to relatively low-frequency range [19]. Tustin differentiator shows a perfect phase response with an ideal 90°, while its magnitude rises to infinite at the Nyquist frequency (i.e., f_s /2 = 5 kHz). This infinite gain will lead to noise amplification and thus is unacceptable.

Naturally, a question coming to mind is whether it is possible for a digital differentiator to combine the advantages of both backward Euler and Tustin differentiators, which means to behave in magnitude as backward Euler differentiator and in phase as Tustin differentiator. An intuitive idea for achieving this goal is to either raise the phase of backward Euler differentiator or attenuate the gain of Tustin differentiator, which, in other words, is to correct their frequency responses to match the ideal differentiator. To do that, a phase-lead compensator is needed for backward Euler differentiator, and for Tustin differentiator, a trap at the Nyquist frequency is expected to cancel out its infinite gain.

B. First-Order Differentiator Based on Backward Euler Plus Lead Compensator

As shown in Fig. 4, the phase lag of backward Euler differentiator $G_{\text{back}}(z)$ is up to 90° at the Nyquist frequency, which is equivalent to a delay of half sampling period. To compensate this half sampling period delay, a lead-lag element [30], a first-order lead compensator [31], [32], and a second-order generalized integrator [33] can be used. Due to its effectiveness and simplicity, the first-order lead compensator is preferred here, and it is expressed as

$$G_{\text{nGI-FOH}}(z) = \frac{(z-1)^2}{zT_s}\cdot Z\left[\frac{G_{\text{nGI}}(s)}{s^2}\right] = \frac{z-1}{T_s}\cdot\frac{z\left[1-e^{-0.5\omega_c T_s}\left(\cos\omega_d T_s + \frac{\omega_c}{2\omega_d}\sin\omega_d T_s\right)\right] - e^{-0.5\omega_c T_s}\left(\cos\omega_d T_s - \frac{\omega_c}{2\omega_d}\sin\omega_d T_s\right) + e^{-\omega_c T_s}}{z^2 - 2ze^{-0.5\omega_c T_s}\cos\omega_d T_s + e^{-\omega_c T_s}}. \tag{9}$$

This article has been accepted for publication in a future issue of this journal, but has not been fully edited. Content may change prior to final publication. Citation information: DOI 10.1109/TPEL.2017.2780174, IEEE Transactions on Power Electronics

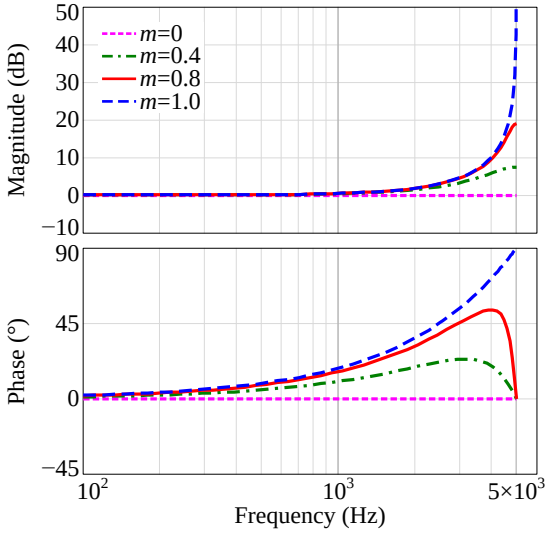

Fig. 5. Frequency response of first-order lead compensator.

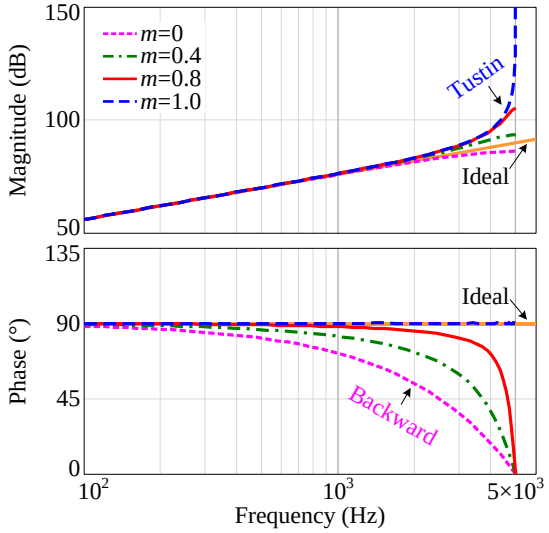

Fig. 6. Frequency response of first-order backward-lead differentiator.

$$G_{\text{lead}}(z)=\frac{(1+m)z}{z+m} \tag{12}$$

where $0 \le m \le 1$. When $m = 0$, $G_{\text{lead}}(z) = 1$; and when $m = 1$, $G_{\text{lead}}(z) = 2z/(z+1)$. Frequency response of $G_{\text{lead}}(z)$ is shown in Fig. 5, where a phase lead is obtained, but the gain at high frequency is amplified as well. A larger m leads to a better compensation of the phase, but a higher amplification of the high-frequency gain. For $m = 1$, a desired phase lead up to 90º is achieved, while an infinite gain appears at the Nyquist frequency. Therefore, a tradeoff between the phase lead compensation and the gain amplification should be made to select a proper m.

Multiplying $G_{\text{back}}(z)$ in (11) and $G_{\text{lead}}(z)$ in (12), a first-order differentiator based on backward Euler plus lead compensator (backward-lead) is constructed, and it is expressed as

$$G_{\text{back-lead}}(z)=G_{\text{back}}(z)\cdot G_{\text{lead}}(z)=\frac{(1+m)}{T_s}\frac{z-1}{z+m}. \tag{13}$$

Note that, for $m = 0$ and $m = 1$, $G_{\text{back-lead}}(z)$ is reduced to $G_{\text{back}}(z)$ and $G_{\text{tustin}}(z)$, respectively. This property is also

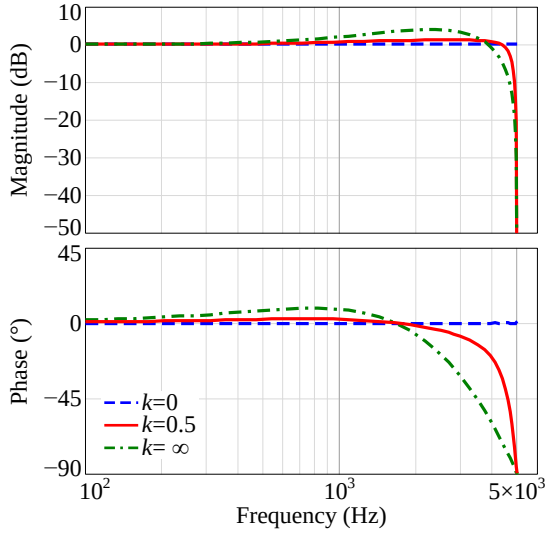

Fig. 7. Frequency response of second-order digital notch filter.

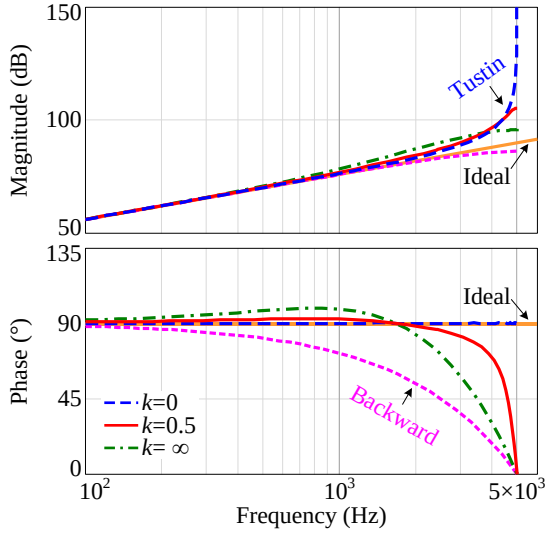

Fig. 8. Frequency response of second-order Tustin-DNF differentiator.

identified in Fig. 6. As seen, $G_{\text{back-lead}}(z)$ behaves more like backward Euler differentiator if m is closer to 0, and more like Tustin differentiator if m is closer to 1. Therefore, $G_{\text{back-lead}}(z)$ can be regarded as a general form of digital differentiator, whose performance can be flexibly adjusted depending on the value of m. Here, $m = 0.8$ is selected as it gives a closer match with the ideal differentiator.

C. Second-Order Differentiator Based on Tustin Plus Digital Notch Filter

For Tustin differentiator, a gain trap at the Nyquist frequency is required, and it can be produced by either a continuous [34] or a digital [35] notch filter. Due to its direct discrete nature, the digital notch filter is preferred here. Recalling $G_{\text{tustin}}(z)$ in (11), it is clear to see that there is a pole located at the Nyquist frequency, i.e.,

$$z=-1=e^{j2\pi\cdot f_s/2\cdot T_s}. \tag{14}$$

Exactly, it is the pole $z = -1$ which causes the infinite gain at the Nyquist frequency. Thus, to cancel out this infinite gain, a zero $z = -1$ should be provided. A second-order digital notch

This article has been accepted for publication in a future issue of this journal, but has not been fully edited. Content may change prior to final publication. Citation information: DOI 10.1109/TPEL.2017.2780174, IEEE Transactions on Power Electronics

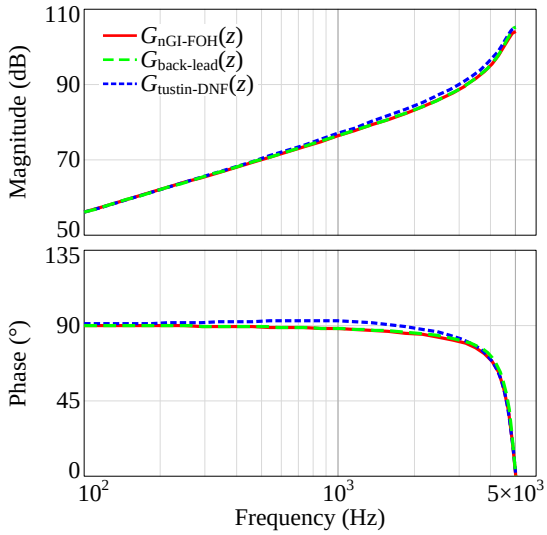

Fig. 9. Frequency responses of nonideal-GI, backward-lead, and Tustin-DNF differentiators.

filter dedicated to this purpose is given as

$$G_{\text{DNF}}(z)=\frac{(k+1)(2z-1)(z+1)}{2(k+1)z^2+z-1}. \tag{15}$$

Owing to its selective filtering characteristic, $G_{\text{DNF}}(z)$ has been widely used in multi-sampled digitally controlled systems for switching-ripple removal [35]. Note that, when k = 0, $G_{\text{DNF}}(z)$ = 1; and when k approaches infinite, $G_{\text{DNF}}(z)$ = $(2z-1)(z+1)/(2z^2)$. Frequency response of $G_{\text{DNF}}(z)$ is shown in Fig. 7, where a gain trap is readily identified. Meanwhile, a phase shift, depending on k, is introduced near the Nyquist frequency. Increasing k doesn't have much effect on the magnitude characteristic, but delays the phase a lot. Therefore, a smaller k (say k = 0.5) is selected to minimize the undesired phase shift.

Multiplying $G_{\text{tustin}}(z)$ in (11) and $G_{\text{DNF}}(z)$ in (15), a second-order differentiator based on Tustin plus digital notch filter (Tustin-DNF) is constructed, and it is expressed as

$$G_{\text{tustin-DNF}}(z)=G_{\text{tustin}}(z)\cdot G_{\text{DNF}}(z)=\frac{2}{T_s}\frac{(k+1)(2z-1)(z-1)}{2(k+1)z^2+z-1}. \tag{16}$$

Obviously, for k = 0, $G_{\text{tustin-DNF}}(z)$ is reduced to $G_{\text{tustin}}(z)$. Frequency response of $G_{\text{tustin-DNF}}(z)$ is shown in Fig. 8, together with those of ideal and backward Euler differentiators for comparison. With k = 0.5, the infinite gain caused by Tustin is clearly flattened, at the cost of a slight phase lag near the Nyquist frequency. This phase lag, although cannot be eliminated, is quite smaller than that of backward Euler differentiator. Therefore, the second-order Tustin-DNF differentiator achieves a good compromise between Tustin and backward Euler differentiators.

It is worth noting that the Tustin-DNF differentiator doesn't show generality as the backward-lead differentiator given in (13), and it is a little more complicated due to the second-order manner. Despite that, the proposing of Tustin-DNF differentiator is still of interest, since it provides a different perspective to cope with the problems faced by conventional differentiators.

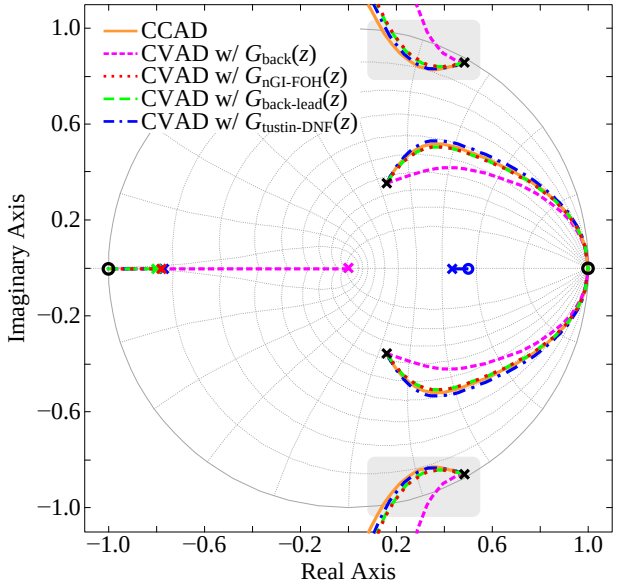

Fig. 10. Root loci of the closed-loop systems by varying the damping gain K_{ad}.

V. Comparison Between Nonideal-GI Differentiator and Proposed Differentiators

For the purpose of the CVAD, the indirect nonideal-GI differentiator has been briefly reviewed, and two direct differentiators, i.e., the first-order backward-lead differentiator and the second-order Tustin-DNF differentiator, have been proposed in the previous sections. In this section, the nonideal-GI differentiator and the proposed ones are compared to help understand the connections and differences between them.

The aforementioned three differentiators, together with their optimum parameters, are given as $G_{\text{nGI-FOH}}(z)$ with ω_c = 5×10^3 rad/s, $G_{\text{back-lead}}(z)$ with m = 0.8, and $G_{\text{tustin-DNF}}(z)$ with k = 0.5, whose frequency responses are redrawn in Fig. 9 for a clear comparison. It is shown that the three differentiators exhibit almost the same derivative characteristics.

This similarity can be better demonstrated with the root locus method. Recalling $T_{ic}(z)$ and $T_{vc}(z)$ in (6), and simplifying the PI regulator $G_i(z)$ to a proportional gain K_p, root loci of the closed-loop systems are plotted by varying the damping gain K_{ad}, as shown in Fig. 10. For the CVAD, the backward Euler, nonideal-GI, backward-lead, and Tustin-DNF differentiators are all evaluated by replacing $G_{\text{d}}(z)$ in $T_{vc}(z)$ with $G_{\text{back}}(z)$, $G_{\text{nGI-FOH}}(z)$, $G_{\text{back-lead}}(z)$, and $G_{\text{tustin-DNF}}(z)$, respectively. The pole movement is obtained with the *LCL* filter parameters listed in Table I, where f_r = 2.27 kHz is higher than $f_s/6$ (1.67 kHz). As shown in the shaded areas, the trajectories of the resonant poles start exactly inside the unit circle, which confirms a stable operation without damping (i.e., K_{ad} = 0) due to $f_r > f_s/6$. With the increase of K_{ad}, the resonant poles first stay inside the unit circle and then track outside. The effective damping regions, within which the resonant poles locate inside the unit circle, are almost identical in the cases of the CCAD and the CVAD with $G_{\text{nGI-FOH}}(z)$, $G_{\text{back-lead}}(z)$, or $G_{\text{tustin-DNF}}(z)$. But for the CVAD with $G_{\text{back}}(z)$, the effective damping region is very narrow, and the resonant

This article has been accepted for publication in a future issue of this journal, but has not been fully edited. Content may change prior to final publication. Citation information: DOI 10.1109/TPEL.2017.2780174, IEEE Transactions on Power Electronics

TABLE I
COMPARISON OF DIFFERENT DIGITAL DIFFERENTIATORS

Features	Backward Euler	High-pass filter	Lead-lag element	Nonideal-GI	Backward-lead	Tustin-DNF
Function order	First order	First order	First order	Second order	First order	Second order
Simplicity	Better	Good	Good	Inferior	Better	Good
Direct discrete development	Yes	No	No	No	Yes	Yes
Effective frequency range	Low	Low	Narrow	Wide	Wide	Wide

poles quickly move outside the unit circle. That means an accurate derivative is performed by any of the nonideal-GI, backward-lead, and Tustin-DNF differentiators, rather than the backward Euler differentiator.

While wondering how the similarity comes from, we can rewrite the nonideal GI $G_{\mathrm{nGI}}(s)$ as

$$G_{\mathrm{nGI}}(s)=\frac{\omega_n^2 s}{s^2+\omega_c s+\omega_n^2} =\frac{\omega_n^2 s}{s^2+\omega_n^2}\cdot\frac{s^2+\omega_n^2}{s^2+\omega_c s+\omega_n^2}=G_{\mathrm{GI}}(s)\cdot G_{\mathrm{CNF}}(s) \tag{17}$$

where $G_{\mathrm{CNF}}(s)$ is a continuous notch filter and expressed as

$$G_{\mathrm{CNF}}(s)=\frac{s^2+\omega_n^2}{s^2+\omega_c s+\omega_n^2}. \tag{18}$$

From (17), it is clear that $G_{\mathrm{nGI}}(s)$ can be regarded as cascading the continuous notch filter $G_{\mathrm{CNF}}(s)$ to the ideal GI $G_{\mathrm{GI}}(s)$. $G_{\mathrm{CNF}}(s)$ aims to trim off the infinite gain caused by $G_{\mathrm{GI}}(s)$, which takes the same effect as that of $G_{\mathrm{DNF}}(z)$ in $G_{\text{tustin-DNF}}(z)$, as shown in (16). Therefore, the essence of the nonideal-GI differentiator can be considered as correcting the frequency response with an embedded filter, which is, in fact, the same as those of the proposed differentiators.

Despite the similarity, it is worth paying more attention on the differences between the nonideal-GI differentiator and the proposed ones. In the nonideal-GI differentiator, the frequency response is corrected in the *s*-domain with the continuous notch filter, which thus calls for a sophisticated discretization method (i.e., FOH) to retain its characteristics in the discrete domain. The proposed differentiators are, however, directly developed in the *z*-domain and corrected with digital filters. The absence of discretization equips the proposed differentiators with the following features.

1) Direct discrete nature. The development of the nonideal-GI differentiator takes two steps: at the first to tune the continuous nonideal GI and then to discretize it. The latter, in particular, is not trivial and would take much effort. As shown in [22] and [23], various discretization methods have to be examined before finding the best one. Comparatively, the natures of the proposed differentiators as direct discrete development make their usages very straightforward.
2) Compact expression. Recalling (9), (13), and (16), it can be seen that the backward-lead differentiator yields a simplest expression due to its first-order manner. However, even with the same second-order property, the expression of the Tustin- DNF differentiator is much more compact than that of the nonideal-GI-based one. The compact expression will facilitate the implementations of the proposed differentiators in a digital signal processor (DSP).
3) Easy algebraic manipulation. As shown in (13) and (16), there are negligible algebraic manipulations in the proposed differentiators. While in the nonideal-GI differentiator, substantial computation efforts have to be devoted to the discretized nonideal GI, due to its complicated symbolic expression, as shown in (9). For simplicity, the computation can be done by using the MATLAB command "c2d" for a specific ω_c.

Based on the previous analysis, a brief summary of the digital differentiators mentioned earlier is given in Table I. It is shown that accurate digital differentiators can be made not only by the indirect discretizing method with a nonideal GI, but also by the direct discretizing method with either backward-lead or Tustin-DNF. These differentiators are therefore competitive in practice. Particularly, the proposed ones are more attractive owing to the aforementioned promising features. Conventional differentiators, namely, the backward Euler, high-pass filter, and lead-lag element differentiators, take effect in either low or narrow frequency range. Despite the inaccuracy, they can still be used in some particular applications. According to their effective frequency ranges, a guideline for selecting the proper digital differentiator is given as follows.

1) If the signal at low frequency needs to be differentiated, such as the derivative feed-forward of grid voltages [36], [37], the backward Euler and high-pass filter differentiators can be chosen.
2) If the signal at a certain frequency needs to be differentiated, such as the CVAD of the *LCL* filter in a stiff grid condition [20], [21], the lead-lag element differentiator, which operates as a selective derivative, can be chosen.
3) If the signal over a wide frequency range needs to be differentiated, such as the CVAD of the *LCL* filter in a weak grid condition (the case studied in this paper), the nonideal-GI, backward-lead, and Tustin-DNF differentiators must be chosen. Among them, the backward-lead differentiator is recommended for its general representation and simplest implementation.

This article has been accepted for publication in a future issue of this journal, but has not been fully edited. Content may change prior to final publication. Citation information: DOI 10.1109/TPEL.2017.2780174, IEEE Transactions on Power Electronics

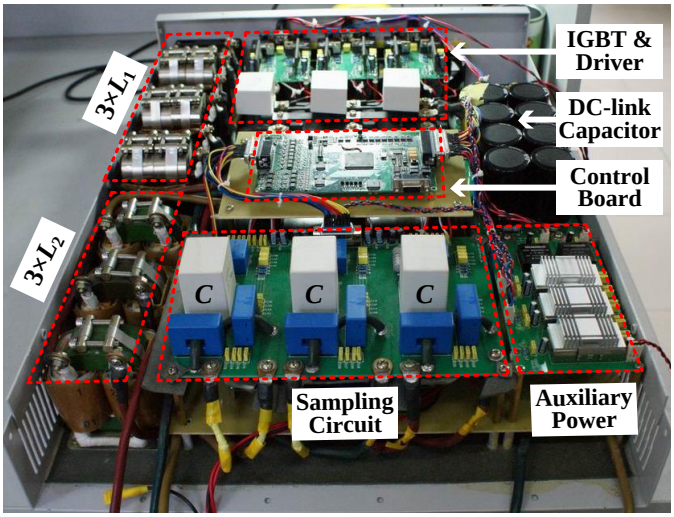

Fig. 11. Photograph of the three-phase grid-connected inverter prototype.

VI. Experimental Verification

A. Experimental Setup

A 12-kW prototype of the three-phase *LCL*-type grid-connected inverter, as shown in Fig. 11, is built and tested in the lab. The inverter bridge is implemented using three IGBT modules (CM100DY-24NF). These modules are driven by M57962L. The capacitor voltage v_C, which is used for the PLL and active damping, is sensed by a voltage hall (LV25-P). The grid current i_2 is sensed by a current hall (LA55-P). The measured signals are sent to an extended 14-bit A/D converter (MAXIM-1324ECM), whose outputs are transmitted to a TI TMS320F2812 DSP for the controller process.

In order to remove the switching noise from the measured signals, a RC low-pass filter with the time constant of 1 μs is installed between the sensors and the A/D converter. Such a filter will also be needed when the capacitor current i_C is directly sensed for active damping. Since its cutoff frequency is much higher than the sampling frequency, this low-pass filter rarely affects the system dynamic performance. Accordingly, it can be omitted from the system model with either CCAD or CVAD.

Table II gives the parameters of the prototype, where the symmetrical regular sampled SVM is implemented. The *LCL* filter is designed with the well-known constraints listed in [38] and [39], and its resonance frequency f_r = 2.27 kHz is kept the same as that in [22] and [23] to provide a comparable basis. For the purpose of active damping, the CCAD and the CVAD with backward Euler, nonideal-GI, backward-lead, and Tustin-DNF differentiators are all tested. The PI parameters are designed with the method in [29], and they are given as K_p = 0.12 and K_i = 60. The optimal damping gain, which yields high robustness against the grid impedance variation, has been derived in [16], and it is calculated as K_{ad} = 0.06 in the test system.

To obtain an intuitive sense, the directly sampled capacitor current and the calculated results by the four differentiators under test are compared, as shown in Fig. 12. For better clarity, the switching ripple of the capacitor current is removed, since it will not be sampled by the synchronous sampling [8]. For any of the nonideal-GI, backward-lead, and Tustin-DNF differentiators, the calculated result is well matched with the sampled result over a wide frequency range. But for the backward Euler differentiator, a visible phase lag is observed in the calculated result as the frequency goes high, which is consistent with the above analysis.

TABLE II
Parameters of the Prototype

Parameter	Symbol	Value	Parameter	Symbol	Value
Input voltage	V_{in}	650 V	Inverter-side inductor	L_1	1300 μH
Grid voltage (RMS)	V_g	220 V	Grid-side inductor	L_2	440 μH
Output power	P_o	12 kW	Filter capacitor	C	15 μF
Fundamental frequency	f_o	50 Hz	Resonance frequency	f_r	2.27 kHz
Switching frequency	f_{sw}	10 kHz	Sampling frequency	f_s	10 kHz

Recalling $T_{ic}(z)$ and $T_{vc}(z)$ in (6), Fig. 13 shows the closed-loop pole maps with L_g varying up to 10% per unit, which equals to 3.8 mH in the test system. For the CCAD, as shown in Fig. 13(a), the resonant poles stay inside the unit circle irrespective of L_g, which implies a robust damping performance as desired. For the CVAD, if the backward Euler differentiator is used, as shown in Fig. 13(b), the resonant poles always stay outside the unit circle, which means the loss of damping effectiveness due to the inaccurate derivative. However, if the backward-lead differentiator is used, as shown in Fig. 13(c), the robust damping matched with the CCAD is recovered, which confirms the accuracy of the proposed differentiator. Similar pole trajectories as Fig. 13(c) can also be obtained with the nonideal-GI and Tustin-DNF differentiators, and they are not repeated here.

B. Experimental Results

Based on the prototype developed above, experimental results are provided here. Fig. 14 shows the experimental results acquired by changing between different active damping solutions at full load. As seen, a stable operation is retained in any of the CCAD and the CVAD with nonideal-GI, backward-lead, and Tustin-DNF differentiators. This is due to the accurate derivatives that ensure an effective damping matched with the CCAD to stabilize the system. However, it is not the case for the CVAD with backward Euler differentiator, where serious oscillation is triggered, due to the large phase lag of backward Euler differentiator that causes the loss of damping effectiveness.

A further comparison of the CCAD and the CVAD with nonideal-GI, backward-lead, and Tustin-DNF differentiators is given in Fig. 15, where the current reference steps between half and full loads. The transient responses in all these cases are almost identical, with a percentage overshoot of 24% and a settling time of 0.8 ms (5% tolerance), which confirms the matched derivative performances of the above three differentiators.

This article has been accepted for publication in a future issue of this journal, but has not been fully edited. Content may change prior to final publication. Citation information: DOI 10.1109/TPEL.2017.2780174, IEEE Transactions on Power Electronics

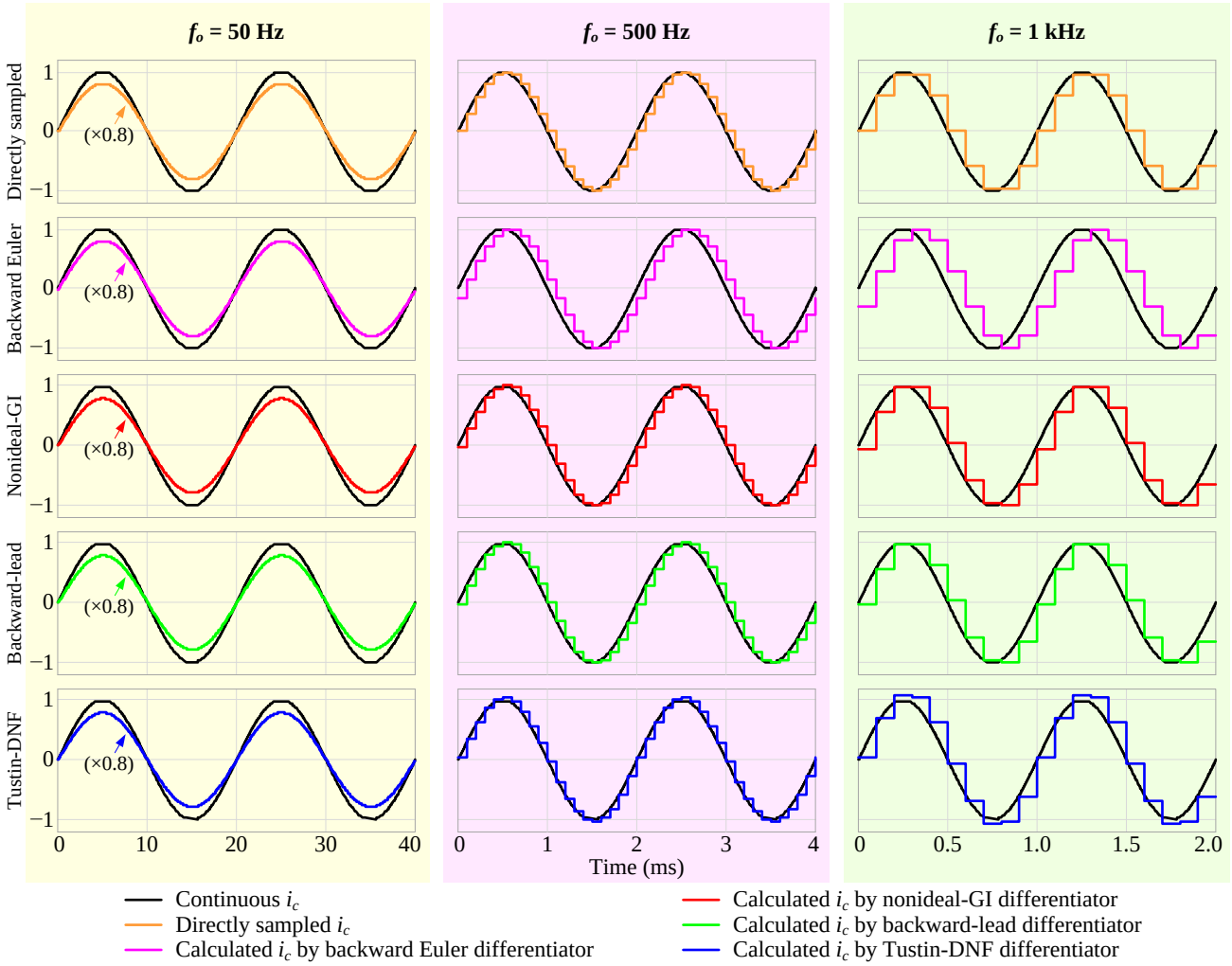

Fig. 12. Simulation results of sampled and calculated capacitor currents under different output frequencies.

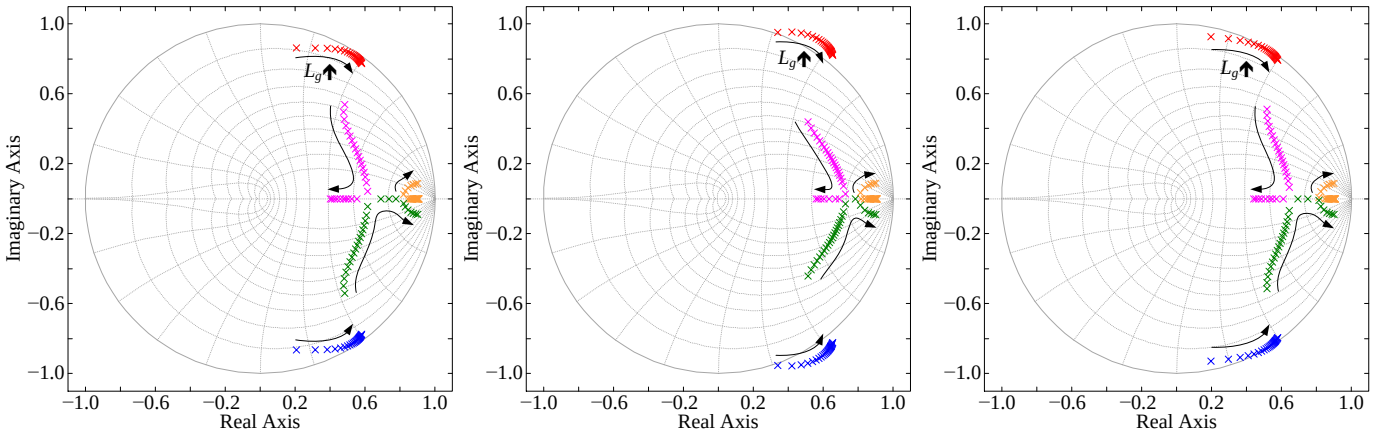

Fig. 13. Closed-loop pole maps with L_g varying up to 3.8 mH. (a) CCAD. (b) CVAD with backward Euler differentiator. (c) CVAD with backward-lead differentiator.

Besides, the operation accuracy of the differentiator is also tested under different switching frequencies. In industrial products, the switching frequency may be adjusted in a certain range according to the load condition. Assuming the variation of ±20%, the switching frequencies ranging from 8 kHz to 12 kHz are considered here. Since the nonideal-GI, backward-lead, and Tustin-DNF differentiators have similar derivative characteristics, the experimental results with the backward-lead differentiator are given as an example, as shown in Fig. 16, where the top figure gives the full view over two fundamental periods and the bottom one gives the zoomed-in view of the shaded area. Satisfactory steady-state operations are preserved under different cases, which imply that the proposed differentiators are less sensitive to the switching frequency variation.

This article has been accepted for publication in a future issue of this journal, but has not been fully edited. Content may change prior to final publication. Citation information: DOI 10.1109/TPEL.2017.2780174, IEEE Transactions on Power Electronics

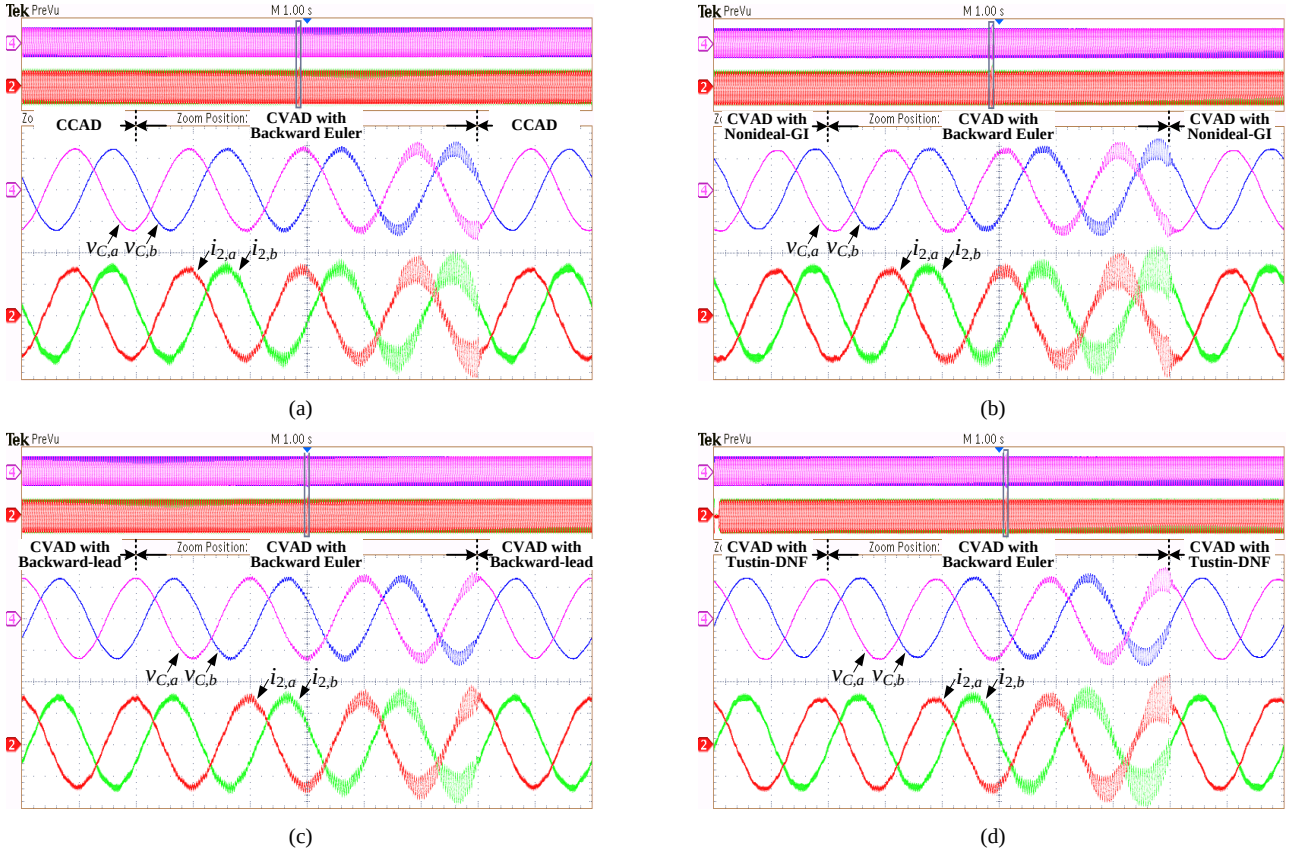

Fig. 14. Experimental results at full load when changing (a) between the CCAD and the CVAD with backward Euler differentiator, and between the CVAD with backward Euler and (b) nonideal-GI, (c) backward-lead, and (d) Tustin-DNF differentiators. Voltage: 250 V/div, current: 20 A/div, time: 10 ms/div.

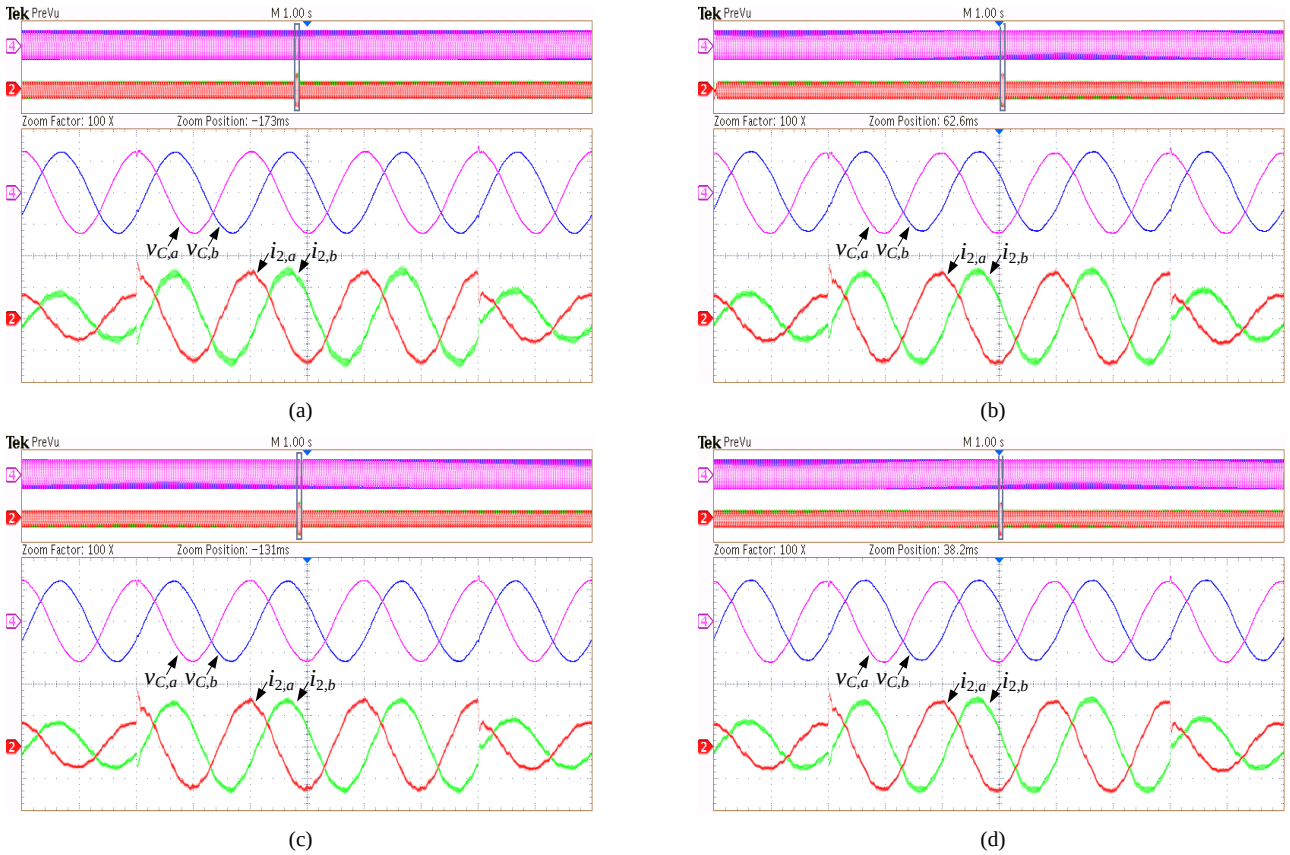

Fig. 15. Experimental results when the current reference steps between half and full loads for (a) the CCAD, (b) the CVAD with nonideal-GI differentiator, (c) the CVAD with backward-lead differentiator, and (d) the CVAD with Tustin-DNF differentiator. Voltage: 250 V/div, current: 20 A/div, time: 10 ms/div.

This article has been accepted for publication in a future issue of this journal, but has not been fully edited. Content may change prior to final publication. Citation information: DOI 10.1109/TPEL.2017.2780174, IEEE Transactions on Power Electronics

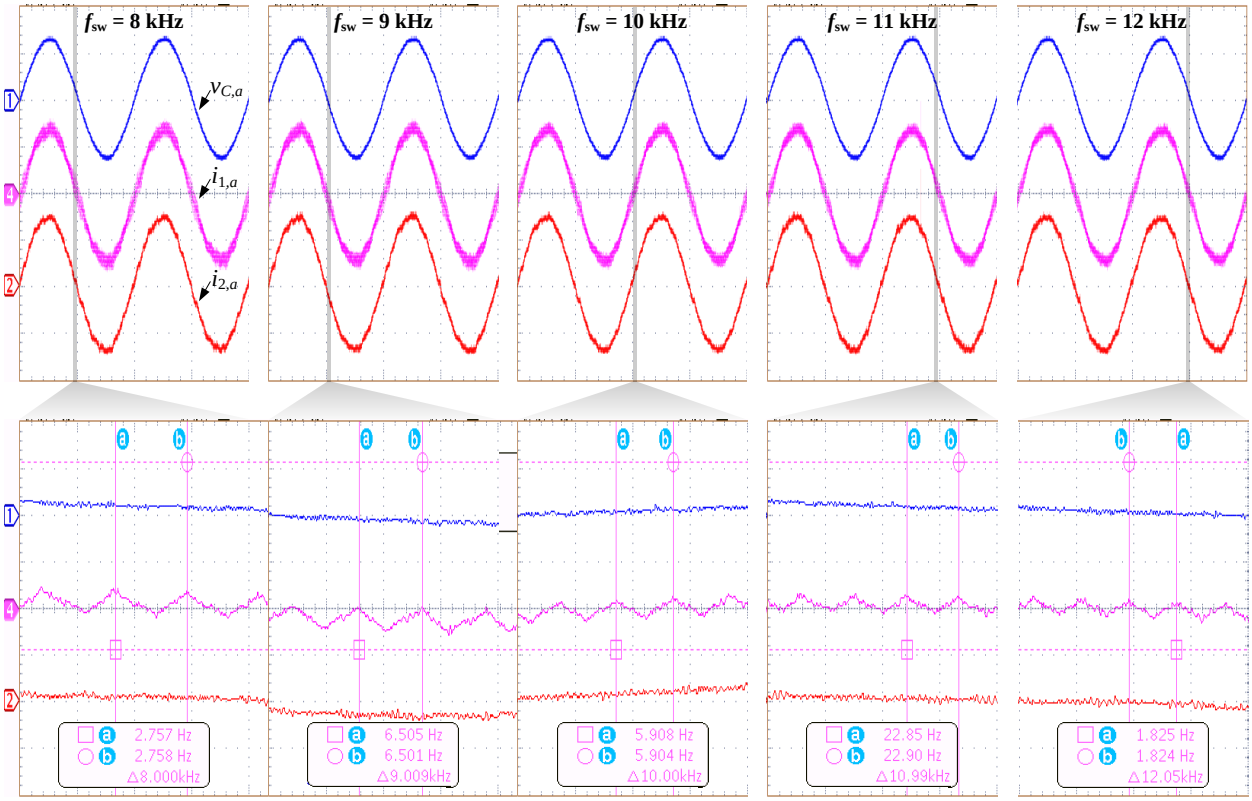

Fig. 16. Experimental results of the CVAD with backward-lead differentiator under different switching frequencies. Voltage: 250 V/div, current: 20 A/div, time: 10 ms/div (top) and 100 μs/div (bottom).

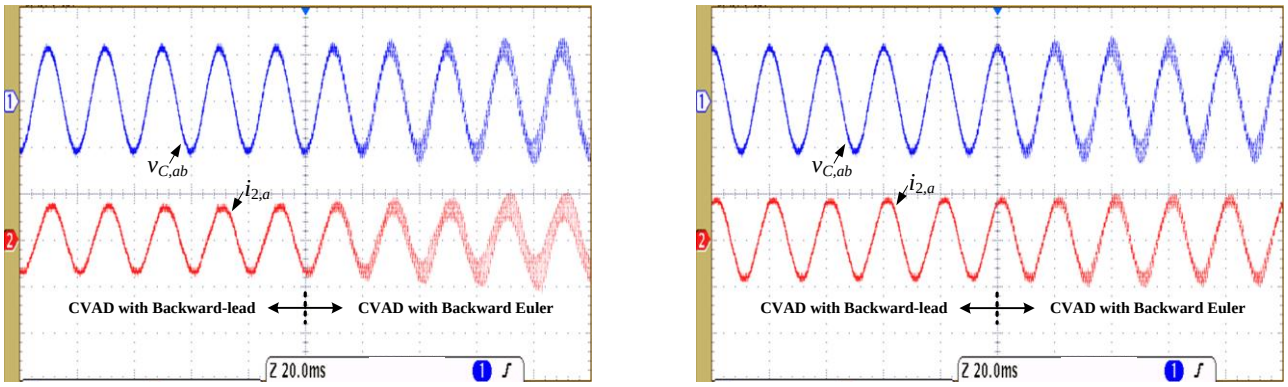

(a) (b)

Fig. 17. Experimental results at full load under grid impedance variation. (a) L_g = 1.9 mH. (b) L_g = 3.8 mH. Voltage: 500 V/div, current: 20 A/div, time: 20 ms/div.

Finally, experiments under the grid impedance variation are performed to verify the system robustness. Two grid inductances, i.e., L_g = 1.9 mH and L_g = 3.8 mH, are tested, as shown in Fig. 17. In either condition, stable operations are retained for the CVAD with backward-lead differentiator, while disastrous oscillations are triggered for the CVAD with backward Euler differentiator. The experimental results show that the proposed differentiators achieve a robust damping performance, which is in agreement with the theoretical analysis in Section VI-A.

VII. Conclusion

Direct realization of digital differentiator in discrete domain has been analyzed in this paper for the capacitor voltage active damping of *LCL*-type grid-connected inverter. A first-order backward-lead differentiator and a second-order Tustin-DNF differentiator are proposed in this manner. The proposed differentiators show the same derivative performance as the well-known nonideal-GI differentiator, and they are more attractive owing to their direct discrete natures, compact expressions, and easy algebraic manipulations. A guideline for selecting the proper digital differentiator is given based on the application scenario. In particular, the first-order backward-lead differentiator is recommended for its general representation and simplest implementation. The outcome of this work allows a digital differentiator to be constructed from a direct discretizing perspective which is usually claimed undesirable. Experimental results from a 12-kW three-phase prototype confirm the theoretical expectations. Except for

active damping, the proposed differentiators can also be used with other applications where derivative is needed.

REFERENCES

[1] X. Ruan, X. Wang, D. Pan, D. Yang, W. Li, and C. Bao, *Control Techniques for LCL-Type Grid-Connected Inverters*. Singapore: Springer, 2017.

[2] R. P. Alzola, M. Liserre, F. Blaabjerg, R. Sebastián, J. Dannehl, and F. W. Fuchs, "Analysis of the passive damping losses in *LCL*-filter-based grid converters," *IEEE Trans. Power Electron.*, vol. 28, no. 6, pp. 2642−2646, Jun. 2013.

[3] R. N. Beres, X. Wang, F. Blaabjerg, M. Liserre, and C. L. Bak, "Optimal design of high-order passive-damped filters for grid-connected applications," *IEEE Trans. Power Electron.*, vol. 31, no. 3, pp. 2083−2098, Mar. 2016.

[4] M. Lu, X. Wang, P. C. Loh, and F. Blaabjerg, "Resonance interaction of multiparallel grid-connected inverters with *LCL* filter," *IEEE Trans. Power Electron.*, vol. 32, no. 2, pp. 894−899, Feb. 2017.

[5] J. He and Y. W. Li, "Generalized closed-loop control schemes with embedded virtual impedances for voltage source converters with *LC* or *LCL* filters," *IEEE Trans. Power Electron.*, vol. 27, no. 4, pp. 1850−1861, Apr. 2012.

[6] X. Wang, Y. W. Li, F. Blaabjerg, and P. C. Loh, "Virtual-impedance-based control for voltage-source and current-source converters," *IEEE Trans. Power Electron.*, vol. 30, no. 12, pp. 7019−7037, Dec. 2015.

[7] Y. Tang, P. C. Loh, P. Wang, F. H. Choo, F. Gao, and F. Blaabjerg, "Generalized design of high performance shunt active power filter with output *LCL* filter," *IEEE Trans. Ind. Electron.*, vol. 59, no. 3, pp. 1443−1452, Mar. 2012.

[8] D. Pan, X. Ruan, C. Bao, W. Li, and X. Wang, "Capacitor-current-feedback active damping with reduced computation delay for improving robustness of *LCL*-type grid-connected inverter," *IEEE Trans. Power Electron.*, vol. 29, no. 7, pp. 3414−3427, Jul. 2014.

[9] L. Harnefors, A. G. Yepes, A. Vidal, and J. D. Gandoy, "Passivity-based controller design of grid-connected VSCs for prevention of electrical resonance instability," *IEEE Trans. Ind. Electron.*, vol. 62, no. 2, pp. 702−710, Feb. 2015.

[10] X. Wang, F. Blaabjerg, and P. C. Loh, "Virtual *RC* damping of *LCL*-filtered voltage source converters with extended selective harmonic compensation," *IEEE Trans. Power Electron.*, vol. 30, no. 9, pp. 4726−4737, Sep. 2015.

[11] X. Li, X. Wu, Y. Geng, X. Yuan, C. Xia, and X. Zhang, "Wide damping region for *LCL*-type grid-connected inverter with an improved capacitor-current- feedback method," *IEEE Trans. Power Electron.*, vol. 30, no. 9, pp. 5247−5259, Sep. 2015.

[12] M. Huang, X. Wang, P. C. Loh, and F. Blaabjerg, "Active damping of *LLCL*-filter resonance based on *LC*-trap voltage or current feedback," *IEEE Trans. Power Electron.*, vol. 31, no. 3, pp. 2337−2346, Mar. 2016.

[13] M. Hanif, V. Khadkikar, W. Xiao, and J. L. Kirtley, "Two degrees of freedom active damping technique for *LCL* filter-based grid connected PV systems," *IEEE Trans. Ind. Electron.*, vol. 61, no. 6, pp. 2795−2803, Jun. 2014.

[14] J. Xu, S. Xie, and T. Tang, "Active damping-based control for grid-connected *LCL*-filtered inverter with injected grid current feedback only," *IEEE Trans. Ind. Electron.*, vol. 61, no. 9, pp. 4746−4758, Sep. 2014.

[15] X. Wang, F. Blaabjerg, and P. C. Loh, "Grid-current-feedback active damping for *LCL* resonance in grid-connected voltage source converters," *IEEE Trans. Power Electron.*, vol. 31, no. 1, pp. 213−223, Jan. 2016.

[16] D. Pan, X. Ruan, C. Bao, W. Li, and X. Wang, "Optimized controller design for *LCL*-type grid-connected inverter to achieve high robustness against grid-impedance variation," *IEEE Trans. Ind. Electron.*, vol. 62, no. 3, pp. 1537−1547, Mar. 2015.

[17] D. Pan, X. Ruan, X. Wang, H. Yu, and Z. Xing, "Analysis and design of current control schemes for *LCL*-type grid-connected inverter based on a general mathematical model," *IEEE Trans. Power Electron.*, vol. 32, no. 6, pp. 4395−4410, Jun. 2017.

[18] M. Liserre, R. Teodorescu, and F. Blaabjerg, "Stability of photovoltaic and wind turbine grid-connected inverters for a large set of grid impedance values," *IEEE Trans. Power Electron.*, vol. 21, no. 1, pp. 263−272, Jan. 2006.

[19] J. Dannehl, F. W. Fuchs, S. Hansen, and P. B. Thøgersen, "Investigation of active damping approaches for PI-based current control of grid-connected pulse width modulation converters with *LCL* filters," *IEEE Trans. Ind. Appl.*, vol. 46, no. 4, pp. 1509−1517, Jul./Aug. 2010.

[20] V. Blasko and V. Kaura, "A novel control to actively damp resonance in input *LC* filter of a three-phase voltage source converter," *IEEE Trans. Ind. Appl.*, vol. 33, no. 2, pp. 542−550, Mar./Apr. 1997.

[21] R. P. Alzola, M. Liserre, F. Blaabjerg, R. Sebastián, J. Dannehl, and F. W. Fuchs, "Systematic design of the lead-lag network method for active damping in *LCL*-filter based three phase converters," *IEEE Trans. Ind. Informat.*, vol. 10, no. 1, pp. 43−52, Feb. 2014.

[22] Z. Xin, X. Wang, P. C. Loh, and F. Blaabjerg, "Realization of digital differentiator using generalized integrator for power converters," *IEEE Trans. Power Electron.*, vol. 30, no. 12, pp. 6520−6523, Dec. 2015.

[23] Z. Xin, P. C. Loh, X. Wang, F. Blaabjerg, and Y. Tang, "Highly accurate derivatives for *LCL*-filtered grid converter with capacitor voltage active damping," *IEEE Trans. Power Electron.*, vol. 31, no. 5, pp. 3612−3625, May. 2016.

[24] S. G. Parker, B. P. McGrath, and D. G. Holmes, "Regions of active damping control for *LCL* filters," *IEEE Trans. Ind. Appl.*, vol. 50, no. 1, pp. 424−432, Jan./Feb. 2014.

[25] C. Zou, B. Liu, S. Duan, and R. Li, "Influence of delay on system stability and delay optimization of grid-connected inverters with *LCL* filter," *IEEE Trans. Ind. Informat.*, vol. 10, no. 3, pp. 1775−1784, Aug. 2014.

[26] J. Wang, J. D. Yan, L. Jiang, and J. Zou, "Delay-dependent stability of single-loop controlled grid-connected inverters with *LCL* filters," *IEEE Trans. Power Electron.*, vol. 31, no. 1, pp. 743−757, Jan. 2016.

[27] X. Wang, F. Blaabjerg, and P. C. Loh, "Passivity-based stability analysis and damping injection for multi-paralleled voltage source converters with *LCL* filters," *IEEE Trans. Power Electron.*, vol. 32, no. 11, pp. 8922−8935, Nov. 2017.

[28] E. Twining and D. G. Holmes, "Grid current regulation of a three-phase voltage source inverter with an *LCL* input filter," *IEEE Trans. Power Electron.*, vol. 18, no. 3, pp. 888−895, May. 2003.

[29] D. G. Holmes, T. A. Lipo, B. P. McGrath, and W. Y. Kong, "Optimized design of stationary frame three phase AC current regulators," *IEEE Trans. Power Electron.*, vol. 24, no. 11, pp. 2417−2426, Nov. 2009.

[30] K. Jalili and S. Bernet, "Design of *LCL* filters of active-front-end two-level voltage-source converters," *IEEE Trans. Ind. Electron.*, vol. 56, no. 5, pp. 1674−1689, May 2009.

[31] C. Chen, J. Xiong, Z. Wan, J. Lei, and K. Zhang, "A time delay compensation method based on area equivalence for active damping of an *LCL*-type converter," *IEEE Trans. Power Electron.*, vol. 32, no. 1, pp. 762−772, Jan. 2017.

[32] M. Lu, X. Wang, P. C. Loh, F. Blaabjerg, and T. Dragicevic, "Graphical evaluation of time-delay compensation techniques for digitally-controlled converters," *IEEE Trans. Power Electron.*, to be published.

[33] Z. Xin, X. Wang, P. C. Loh, and F. Blaabjerg, "Grid-current-feedback control for *LCL*-filtered grid converters with enhanced stability," *IEEE Trans. Power Electron.*, vol. 32, no. 4, pp. 3216−3228, Apr. 2017.

[34] J. Dannehl, M. Liserre, and F. W. Fuchs, "Filter-based active damping of voltage source converters with *LCL* filter," *IEEE Trans. Ind. Electron.*, vol. 58, no. 8, pp. 3623−3633, Aug. 2011.

[35] L. Corradini, P. Mattavelli, E. Tedeschi, and D. Trevisan, "High-bandwidth multisampled digitally controlled DC-DC converters using ripple compensation," *IEEE Trans. Ind. Electron.*, vol. 55, no. 4, pp. 1501−1508, Apr. 2008.

[36] X. Wang, X. Ruan, S. Liu, and C. K. Tse, "Full feedforward of grid voltage for grid-connected inverter with *LCL* filter to suppress current distortion due to grid voltage harmonics," *IEEE Trans. Power Electron.*, vol. 25, no. 12, pp. 3119−3127, Dec. 2010.

[37] W. Li, X. Ruan, D. Pan, and X. Wang, "Full-feedforward schemes of grid voltages for a three-phase *LCL*-type grid-connected inverter," *IEEE Trans. Ind. Electron.*, vol. 60, no. 6, pp. 2237−2250, Jun. 2013.

[38] D. Pan, X. Ruan, C. Bao, W. Li, and X. Wang, "Magnetic integration of the *LCL* filter in grid-connected inverters," *IEEE Trans. Power Electron.*, vol. 29, no. 4, pp. 1573−1578, Apr. 2014.

[39] R. N. Beres, X. Wang, M. Liserre, F. Blaabjerg, and C. L. Bak, "A review of passive power filters for three-phase grid connected voltage-source converters," *IEEE J. Emerg. Sel. Topics Power Electron.*, vol. 4, no. 1, pp. 54−69, Mar. 2016.

Donghua Pan (S'12-M'15) was born in Hubei Province, China, in 1987. He received the B.S. and Ph.D. degrees in electrical engineering from Huazhong University of Science and Technology, Wuhan, China, in 2010 and 2015, respectively.

From July 2015 to August 2017, he was a Research Engineer with Suzhou Inovance Technology Co., Ltd., Suzhou, China. Since September 2017, he has been with Aalborg University, Aalborg, Denmark, where he is currently a Postdoctoral Fellow in the Department of Energy Technology. His research interests include magnetic integration technique and renewable energy generation system.

Xinbo Ruan (M'97-SM'02-F'16) was born in Hubei Province, China, in 1970. He received the B.S. and Ph.D. degrees in electrical engineering from Nanjing University of Aeronautics and Astronautics (NUAA), Nanjing, China, in 1991 and 1996, respectively.

In 1996, he joined the Faculty of Electrical Engineering Teaching and Research Division, NUAA, where he became a Professor in the College of Automation Engineering in 2002 and has been engaged in teaching and research in the field of power electronics. From August to October 2007, he was a Research Fellow in the Department of Electronic and Information Engineering, Hong Kong Polytechnic University, Hong Kong, China. From 2008 to 2011, he was also with the School of Electrical and Electronic Engineering, Huazhong University of Science and Technology, Wuhan, China. He is a Guest Professor with Beijing Jiaotong University, Beijing, China, Hefei University of Technology, Hefei, China, and Wuhan University, Wuhan, China. He is the author or coauthor of 9 books and more than 200 technical papers published in journals and conferences. His main research interests include soft-switching dc-dc converters, soft-switching inverters, power factor correction converters, modeling the converters, power electronics system integration and renewable energy generation system.

Dr. Ruan received the Delta Scholarship by the Delta Environment and Education Fund in 2003 and the Special Appointed Professor of the Chang Jiang Scholars Program by the Ministry of Education, China, in 2007. From 2005 to 2013, he served as Vice President of the China Power Supply Society, and from 2014 to 2016, he served as Vice Chair of the Technical Committee on Renewable Energy Systems within the IEEE Industrial Electronics Society. He is currently an Associate Editor for the IEEE TRANSACTIONS ON INDUSTRIAL ELECTRONICS, IEEE JOURNAL OF EMERGING AND SELECTED TOPICS IN POWER ELECTRONICS, IEEE TRANSACTIONS ON POWER ELECTRONICS, and IEEE TRANSACTIONS ON CIRCUITS AND SYSTEMS—II: EXPRESS BRIEFS.

Xuehua Wang (M'12) was born in Hubei Province, China, in 1978. He received the B.S. degree in electrical engineering from Nanjing University of Technology, Nanjing, China, in 2001, and the M.S. and Ph.D. degrees in electrical engineering from Nanjing University of Aeronautics and Astronautics, Nanjing, China, in 2004 and 2008, respectively.

He is currently an Associate Professor in the School of Electrical and Electronic Engineering, Huazhong University of Science and Technology, Wuhan, China. His main research interests include multilevel inverter and renewable energy generation system.